SUPPLEMENTARY INFORMATION OF: Quantum Sensing of Magnetic Fields with Molecular Spins

Claudio Bonizzoni[1,2*], Alberto Ghirri[2], Fabio Santanni[3], and Marco Affronte[1,2]

[1]Dipartimento di Scienze Fisiche, Informatiche e Matematiche Università di Modena e Reggio Emilia, via G. Campi 213/A, 41125, Modena, Italy
[2]CNR Istituto Nanoscienze, Centro S3, via G. Campi 213/A, 41125, Modena, Italy.
[3]Dipartimento di Chimica Ugo Schiff Universitá degli Studi di Firenze, via della Lastruccia 3, 50019, Sesto Fiorentino (FI), Italy.
[*]mail to: claudio.bonizzoni@unimore.it

April 1, 2024

Contents

1 Supplementary Methods

1.1 Combined MW and RF Spectrometer

The spectrometer used is shown in Supplementary Fig. 1. This is essentially based on the microwave (MW) heterodyne spectrometer previously reported in [1, 2], in which one channel of the Arbitrary Waveform Generator (AWG) is used to generate the MW excitation tone through frequency upconversion. The other channel is used to generate a radiofrequency (RF) excitation which is routed directly to the copper coil with a dedicated RF coaxial line. This way the setup can generate synchronized MW and RF pulse sequences in which each pulse parameter

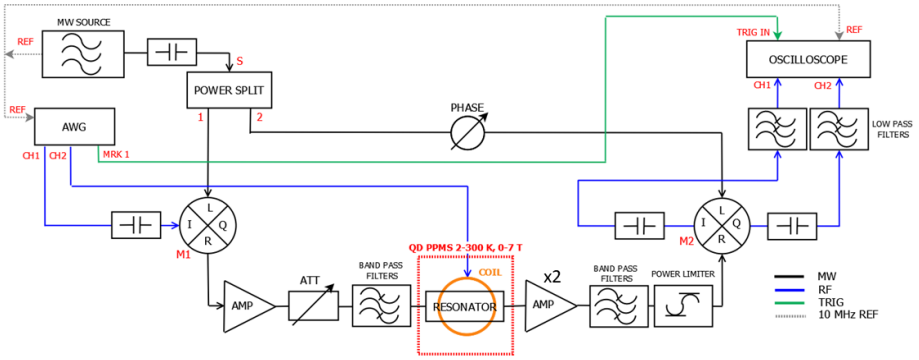

Supplementary Figure 1: The spectrometer used is based on one previously reported in [1, 2] in which Channel 2 of the Waveform Generator is routed directly to the radiofrequency (RF) coil by means of a dedicated RF coaxial line added on the low temperature probe.

(amplitude, duration, phase, interpulse delay) can be adjusted. The readout is performed at MW frequency and in time domain with an oscilloscope, after the output MW signal has been downconverted with a second mixer. The generation of the two excitations and acquisition are controlled by a home-written Python script.

1.2 Calibration of the RF magnetic field

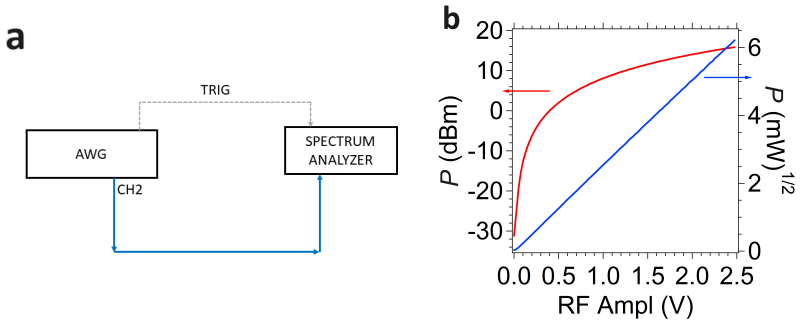

Supplementary Figure 2: a) Setup used for measuring the RF power generated at AWG port. b) Power measured as a function of the RF amplitude on the AWG port going to the coil.

The calibration of the RF magnetic field generated by the coil is done by estimating the power reaching the sample position. To this end, we first check the output power provided by the AWG at its output port feeding the coil, as in Fig. 2. Here, a spectrum analyzer is used in zero bandwidth mode and set to the RF frequency of the modulation, and it's triggered directly by the AWG. The same sensing protocol used for experiments is played on AWG. The output power quadratically increases with the RF amplitude, as expected (blue trace).

Then, we measure the transmission from the AWG output port through the coil, a pick-up YBCO/Sapphire microstrip transmission line (width $w = 400\,\mu$m) and the output microwave line [3, 4], as in Fig. 3.a. Again, the same protocol for MW and RF excitation used during experiments is applied. The transmission is measured in time domain with an oscilloscope and is given by the ratio between the output signal amplitude and its corresponding input amplitude measured on AWG port. Here we note that this characterization is similar to the internal operation done by a Network Analyzer to measure the scattering parameters of an electrical network.

However, time domain measure has been preferred for two main reasons: i) the experimental protocol is performed in time domain, and ii) the RF frequency is below the lower limit of the acquisition bandwidth of our Network Analyzer, preventing from a Continuous Wave characterization. The attenuation of each part of the input RF line, of the YBCO transmission line mounted inside its shielding box, and of the output MW line has been measured with a similar method (Fig. 3.b).

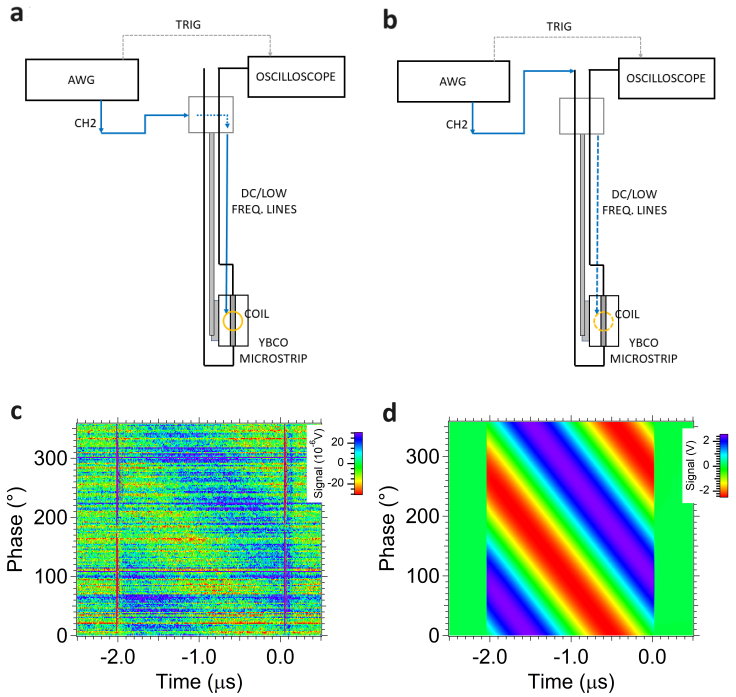

Supplementary Figure 3: a,b) Sketches of the set ups used for the calibration of the magnetic field generated by the coil (a) and of the input and output coaxial lines (b). The transmission from AWG to coil and, then, to output microwave transmission line through a pick YBCO microstrip broadband transmission line is measured in time domain with an oscilloscope. A similar method is done also for the coaxial lines. c,d) Example of calibration signal obtained for a RF phase sweep with $V_{\mathrm{RF}} = 2.5\,\mathrm{V}$ (c) and of its corresponding input signal on AWG (d).

Once input attenuation is known the power reaching the coil can be calculated. Once all output attenuation are known, also the power picked-up by the microstrip line can be evaluated. Finally, the power reaching the microstrip can be related to the electromagnetic energy released into the effective sensitive volume of the microstrip (V_{eff}) and, then, to the magnitude of the RF magnetic field according to equation 1:

$$E = \int_0^{2\tau} P(t)dt = 2u_{\mathrm{B}}\, V_{\mathrm{eff}} = \frac{B_{\mathrm{RF}}^2}{\mu_0}\, V_{\mathrm{eff}}. \tag{1}$$

Here $u_B = \frac{B_{\mathrm{RF}}^2}{2\mu_{\mathrm{B}}}$ is the magnetic energy density, $V_{\mathrm{eff}} = w_{\mathrm{eff}}\, \Phi_{\mathrm{coil}}\, h_{\mathrm{eff}}$ is a volume in which the signal pick from the coil is effective. This is estimated considering and effective width $w_{\mathrm{eff}} = 0.7\,\mathrm{mm}$, a length equal to the diameter of the coil $\Phi_{\mathrm{coil}} = 5\,\mathrm{mm}$ and an effective height $h_{\mathrm{eff}} = 1\,\mathrm{mm}$ from the surface of the strip. The integral in Eq. 1 is calculated form the power dependence $P(t)$ obtained from the spectrum analyzer. The magnetic field generated by the coil at sample position is finally given by Eq. 2:

$$B_{\mathrm{RF}} = \sqrt{\frac{\mu_0 P_{\mathrm{avr}} 2\tau}{w_{\mathrm{eff}}\, \Phi_{\mathrm{coil}}\, h_{\mathrm{eff}}}}, \tag{2}$$

where the integral has been replaced by its average power value, P_{avr}, multiplied by the total RF duration, 2τ. Results are shown in Fig. 4. The maximum field amplitude is on the order of few gauss and can reach up to ≈ 1 mT. The conversion between the voltage amplitude applied and the corresponding RF field amplitude generated by the coil is given by $\frac{dB_{\mathrm{RF}}}{dV_{\mathrm{RF}}} = 7.5 \cdot 10^{-4}\,\mathrm{T\,V^{-1}}$.

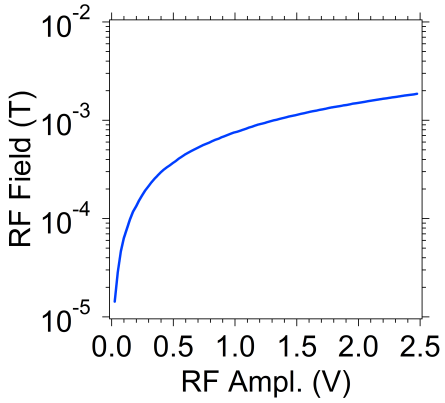

Supplementary Figure 4: Conversion between the RF voltage amplitude on the output port of AWG and the amplitude of the RF magnetic field generated by the coil at the sample position.

We finally assume that, due to the small dimension of the sample with respect to the microstrip length, the values reported in Supplementary Fig. 4 correspond to the ones applied at sample position. The method described above ensures that the experimental configuration, the geometry and the relative orientation of the oscillating fields are similar to the ones used for experiments, and that the estimated RF field is the one felt by the spin ensemble in its final position.

2 Supplementary Figures

2.1 Continuous-Wave Spectroscopy for VO(TPP) and BDPA

We report in Supplementary Fig. 5 the Continuous-Wave transmission spectroscopy performed on VO(TPP) and on BDPA samples. VO(TPP) crystal shows 8 lines, as expected from the VO^{2+} moiety and consistently to what previously reported in [2]. BDPA shown a main signal at $g \approx 2$, which results from the convolution of two lines, consistently to what previously reported in [3].

We fit the frequency as a function of the static magnetic field using Eq. 3, which is based on a lumped-element model treating the coupled resonator-ensemble as a set of coupled harmonic oscillators (one resonator coupled to a number #line of independent spin signals) [3, 4]. This way, the magnetic coupling of each j^{th} is fully characterized by its coupling rate to the resonator, Ω_j, and by its linewidth, γ_j. The coupling rate is related to the single spin coupling rate, $\Omega_{\mathrm{S},j}$, and to the effective number of spins, N_{eff}, by: $\Omega_j = \Omega_{\mathrm{S},j}\sqrt{N_{\mathrm{eff}}}$.

$$\nu = \nu_0 + \sum_{j=1}^{\#\mathrm{lines}} \frac{\Omega_j^2(\nu_0 - \nu_{\mathrm{S},j})}{(\nu_0 - \nu_{\mathrm{S},j})^2 + \gamma_j^2} \tag{3}$$

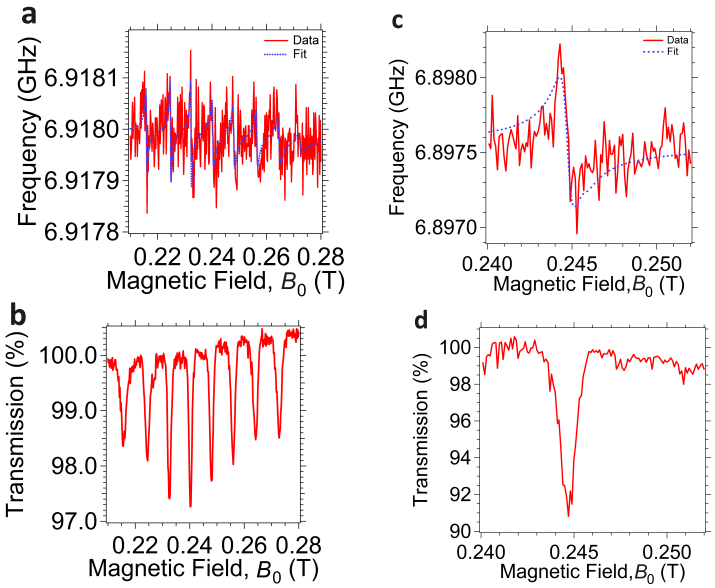

Supplementary Figure 5: Continuous-Wave transmission spectroscopy performed on the molecular spin ensemble through the coplanar resonator at low temperature. The frequency and the normalized transmission of the resonator are shown as a function of the static magnetic field, B_0 for both VO(TPP) (a,b) and BDPA (c,d). Dashed lines is a fit obtained with Eq. 3 [3, 4].

The fit for VO(TPP) is done using 8 different lines, one for each signal measured. The fourth line, which is the one used for experiments, gives $\Omega = 1.3 \pm 0.5$ MHz and $\gamma = 12 \pm 3$ MHz. The fit for BDPA gives $\Omega = 3.3 \pm 0.5$ MHz and $\gamma = 12.5 \pm 2$ MHz for each of the two lines giving the main signal. Stating from these values the estimated effective spin number results $N_{\text{eff}} = 4.3 \cdot 10^{14}$ spins for VO(TPP) (using $\Omega_S = 0.5/8$ Hz) and $N_{\text{eff}} = 4.4 \cdot 10^{13}$ spins for BDPA (using $\Omega_S = 0.5$ Hz) at low temperature. The number of spins taking part to the echo is evaluated considering the fraction of the spin spectral density excited by the bandwidth resulting from the combination of the bandwidth of both resonator and $\pi/2$ pulse [3]. The number of spin results $N_{\text{echo}} = 3.5 \cdot 10^{13}$ for VO(TPP) and $N_{\text{echo}} = 5.4 \cdot 10^{12}$ for BDPA.

2.2 Dynamical Decoupling on BDPA without RF Modulation

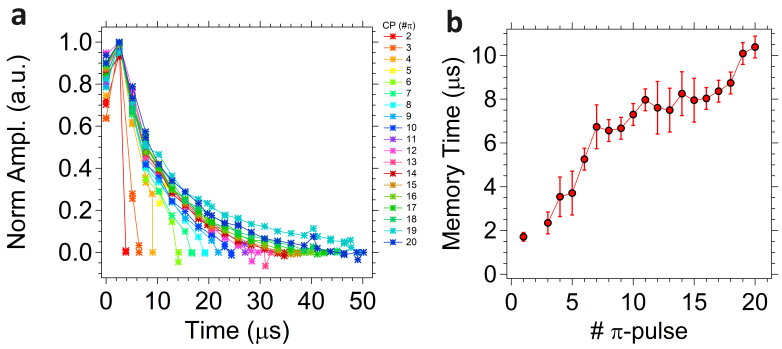

Supplementary Figure 6: a) Normalized echo amplitude extracted from the Carr-Purcell-Meiboom-Gill sequence as a function of the relative time at which they are observed for the BDPA sample without RF coil. The number of π pulses used is reported in the legend. b) Memory time extracted from left as a function of the number of π pulses.

We show in Supplementary Fig. 6 the result of a Carr-Purcell-Meiboom-Gill sequence applied to BDPA in an independent sample characterization performed at 3 K on the coplanar resonator without RF coil. The sequence consists of a first $\pi/2$ pulse, followed by a interpulse delay time $\tau = 1200\,\text{ns}$ and, then, by a train of π pulses equally spaced by 2τ. The sequence is followed by a relaxation time $t_{\text{relax}} = 25\,\text{ms}$ [2]. An echo signal is measured at a delay τ after each π pulse of the protocol, even after up to 20 π pulses are applied. The memory time is then extracted from the decay of the echo amplitude as a function of their relative time with respect to the first echo by using a stretched exponential decay in the form $A(t) = A_{\text{baseline}} + A(t_0)e^{-(\frac{t-t_0}{T_{\text{m}}})^x}$. The resulting memory time are reported in Supplementary Fig. 6.b as a function of the number of π pulses. A value up to $15\,\mu\text{s}$ ($\approx$ 10 time the Hahn echo memory time) is found at 3 K using 20 π pulses. The absence of a saturation value suggests that further enhancement could be achieved with a larger number of pulses. The possibility to extend the coherent manipulation well beyond simple Hahn Echo sequence (in principle up to a total free precession time of $2\tau(\#\pi - 1) + 2\tau = 2\tau(\#\pi) = 2 \cdot 1200 \cdot 20\,ns = 48\,\mu\text{s}$, being $\#\pi$ the number of π pulses) makes BDPA an interesting playground for studying the RF sensing during Dynamical Decoupling protocols.

2.3 Effect of interpulse delay on Hahn Echo sensing protocol for VO(TPP)

We investigate the effect of the interpulse delay, τ, on the Hahn echo protocol using the VO(TPP) sample. Results for an amplitude sweep (at fixed $\phi_{\text{RF}} = 0°$) are shown in Supplementary Fig. 7.a. The phase of the echo shows a change from $-90°$ to $90°$, which occurs at lower applied RF amplitudes as τ is increased. This is consistent with the larger phase accumulation given by the longer time available for the RF modulation to act on spins, according to Eq. (2) of main text. Furthermore, a slight increase in the slope of the phase as a function of RF amplitude is visible, suggesting that the transduction from RF magnetic field into phase is more efficient. Similar trends are observed when the RF phase is swept between 0° and 360° for fixed $B_{1,\text{RF}} = 1.83\,\text{mT}$ (Supplementary Fig. 7.b). Increasing τ gives more phase accumulation, as evidenced by the increasing number of jumps between $-90°$ to $90°$. At the same time too long τ values with respect to the memory time will introduce more noise into the signals (purple trace), bringing to a progressive loss of phase coherence of spin precession.

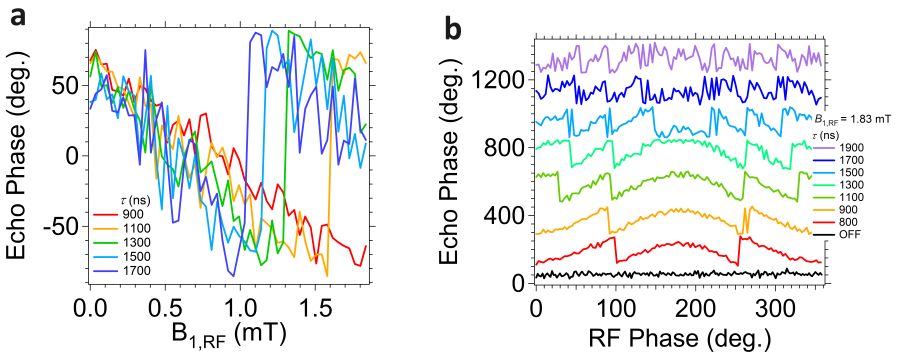

Supplementary Figure 7: a) Echo phase extracted from Hahn echo sequence as a function of the RF field amplitude for different interpulse delays τ (between $\tau = 900$ and $\tau = 1700$ ns, see legend). b) Echo phase extracted from Hahn echo sequence as a function of the RF phase for different interpulse delays τ (between $\tau = 900$ and $\tau = 1900$ ns, see legend) at fixed $B_{1,\text{RF}} = 1.83\,\text{mT}$. Vertical offset is added for better clarity.

2.4 Hahn echo sensing protocol for BDPA

We repeat the Hahn echo sensing experiment described in the main text for the BDPA sample. We first fix again $n = 1$ and $\phi_{\mathrm{RF}} = 0°$ in Eq. (2) of main text, and we increase the RF field amplitude step-by-step. Two different trends are visible as a function of the RF amplitude (Supplementary Fig. 8). A linear phase response is visible between 0 and up to $\approx 4 \cdot 10^{-4}\,\mathrm{T}$, value at which the echo signal is almost entirely suppressed. This behaviour is inline with what observed for VO(TPP). A further increase in the RF amplitude brings to a small revival of the echo amplitude up to $\approx 1.1\,\mathrm{mT}$ and then to another monotonic decrease. In this latter range the dependence of the echo phase by the applied RF deviates form a linear behaviour. We attribute this effect to the fact that the echo amplitude is now vanishing and the RF signal cannot be considered as a small perturbation on it. This situation is similar to the case of variance detection, in which the phase variation is proportional to a power of the probed quantity [5]. Under our experimental conditions, the exponent results to be between 1 and 2 for $0.8\,m\mathrm{T} \leq B_{1,\mathrm{RF}} \leq 1.2\,m\mathrm{T}$ and becomes equal to 2 for $B_{1,\mathrm{RF}} \geq 1.2\,m\mathrm{T}$ (see Supplementary Fig. 8).

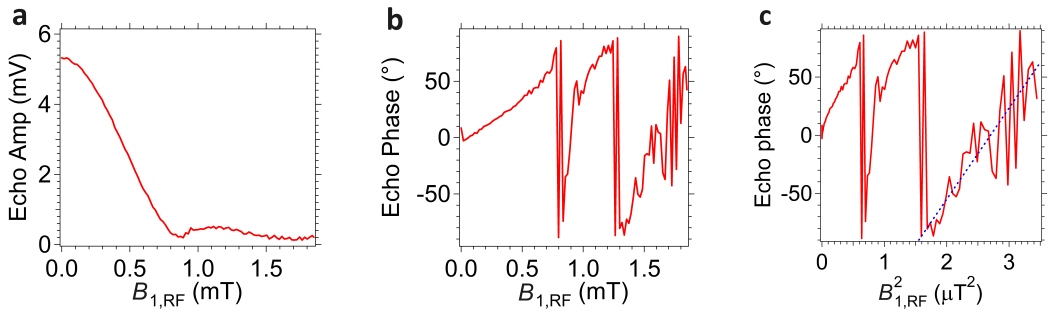

Supplementary Figure 8: Echo amplitude (a) and phase (b) for the Hahn echo signal of BDPA as a function of the RF field amplitude. The phase of the output echo is again wrapped between -90 and 90 degrees for better clarity. c) Echo phase as a function of the squared RF field amplitude. Blue dashed line is a linear fit.

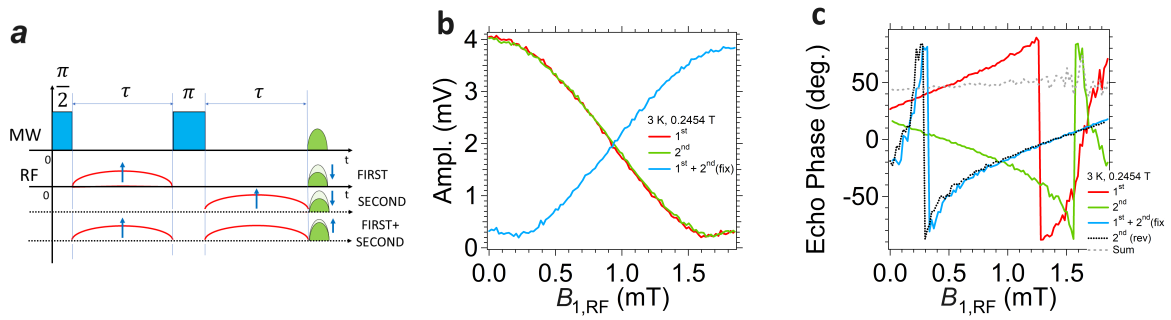

Supplementary Figure 9: Echo amplitude (b) and phase (c) extracted from Hahn echo signal of BDPA as a function of the RF field amplitude. The phase of the output echo, which is wrapped between -90 and 90 degrees for better clarity. The RF modulation is applied only during first (red) or second (green) interpulse delay or, conversely, is applied of both delays (light-blue trace). The sketch of the RF modulations applied (a), same of Fig. 3.e of main text, is added for better clarity.

We then repeat the experiment shown in Fig. 3.e,f of main paper, in which the RF modulation is applied only on the first, the second or both free precession times (Supplementary Fig. 9). Applying the RF modulation only on one of the two interpulse delays reduces echo amplitude

(red and green traces), giving two phase shifts with opposite sign. The spin echo is progressively silenced by the presence of the RF modulation. Conversely, if the RF modulation is fixed during the second τ ($B_{1,\mathrm{RF}} = 1.83\,\mathrm{V}$, $\phi_{\mathrm{RF}} = 0°$) and the RF amplitude is gradually added on the first one, the initial (unperturbed) echo amplitude is progressively recovered (light-blue trace). This suggests that the two RF modulation are progressively cancelling each other. One can realize that the phase variation as a function of $B_{1,\mathrm{RF}}$ for this latter case (light-blue trace) is exactly the reversed image of the one obtained for the sweep over the second τ (black dashed trace, to be compared with green one). This is consistent with the fact that if the first modulation is progressively added, the effect of the second one gradually reduces in the same way which would be achieved by reducing its RF amplitude (*i.e.* moving from 1.83 mT down to zero along green trace). This is also corroborated by the fact that the sum of the individual phase variations (dashed gray trace, resulting from the sum of red and green ones) remains constant as a function of $B_{1,\mathrm{RF}}$. These result corroborates the algebraic additivity of the modulations over the two different τ, as shown also in the main text.

2.5 Dynamical Decoupling Sensing protocol for BDPA

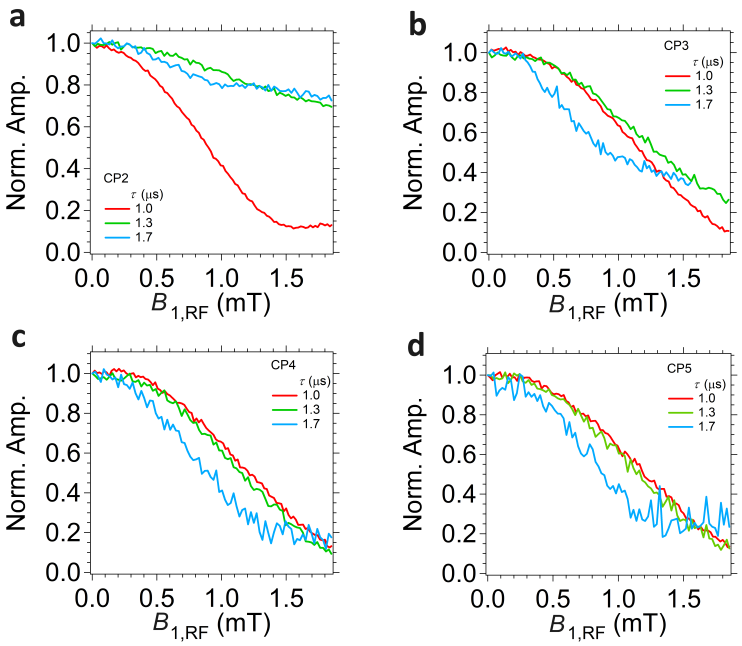

Supplementary Figure 10: Sensing RF field with Carr-Purcell-Meiboom-Gill sequence for different interpulse delay values. Echo amplitude as a function of RF field amplitude for different interpulse delays ($\tau = 1.0, 1.3, 1.7\,\mu$s, see legends) are shown for different number of π pulses used (2 up to 5, from (a) to (d)).

We investigate the effect of different number of π pulses and interpulse delays on RF sensing. This is because, as discussed in the main text, applying a Dynamical Decoupling protocol is equivalent to introduce a bandpass frequency filter to the environment acting on spins during their free precession [5, 6, 7]. This filtering behaviour is usually exploited for increasing the spin memory time (Supplementary Fig. 6) but it can affect also the sensitivity to an AC modulation applied to the sequence [8, 9]. Supplementary Fig. 10 shown our results for different interpulse delays ($\tau = 1, 1.3, 1.7\,\mu$s, corresponding to $\nu_{RF} = 1, 0.77, 0.59$ MHz respectively) and number of π pulses (from 2 up to 5). The effect of modulation with the largest frequency (lowest τ) is more evident for CP2 sequence and it gradually reduces if the number of pulses is increased.

The upper limit is reached for $B_{1,\mathrm{RF}} = 1.83\,\mathrm{mT}$, limited by our set up, suggesting that reaching a similar effect would require the use of much larger RF magnetic field values. Conversely, the effect observed for the lowest frequency value on echo amplitude progressively increases if the number of pulses is increased. A lower limit is reached by the amplitude value. For that specific choice of parameters, larger effect is not expected if the RF amplitude is further increased.

3 Supplementary Discussion

3.1 Estimation of the Number of Spins

We first estimate the effective number of spins coupled by the resonator mode volume starting from fits of the Continuous-Wave transmission spectroscopy performed through the resonator (Sec. 2.1), similarly to what previously reported in [3, 2]. The number of spins taking part to the echo, which also gives an estimation of the "size" of our sensing element, is then evaluated as described in Sec. 2.1. The main results are summarized in Tab. 1.

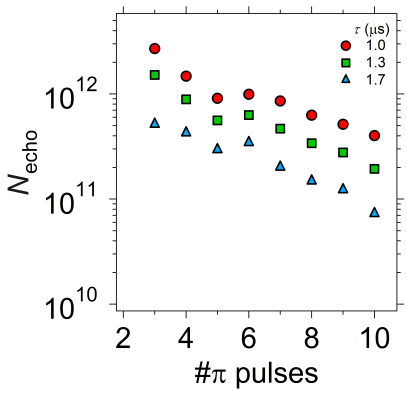

Supplementary Figure 11: Estimation of the number of spins remaining in the last echo of the CP train as a function of the number of π pulses used for the sequence.

Sample	$T(K)$	N_{eff}	N_{echo}
VO(TPP)	4	$4 \cdot 10^{14}$	$3.5 \cdot 10^{13}$
BDPA	3	$4.4 \cdot 10^{13}$	$5.4 \cdot 10^{12}$

Supplementary Table 1: Effective number of spins (N_{eff}) and number of spin taking part to the Hahn Echo (N_{echo}) evaluated for the experiments reported in Sec. 2.1.

We estimate the number of spin remaining in the last echo of the CP sequence considering that, for a given number of π pulses and τ value, the expected memory time (Supplementary Fig. 6) and the total duration of the sequence t_{seq} are known. Since the echo intensity is proportional to the residual magnetization in the precession plane, *i.e.* to the number of preceeding spins, we can expect the number of spins to decays as $N_{\mathrm{echo},\#\pi} = N_{\mathrm{echo}} e^{-(\frac{t_{\mathrm{seq}}}{T_{\mathrm{m},\#\pi}})^{x_{\#\pi}}}$. This give the estimations reported in Supplementary Fig. 11.

3.2 Estimation of the Spin Sensitivity

Hahn Echo Sensing Protocol We estimate the spin sensitivity according to the definition reported in [10], *i.e.* the minimum quantity (here RF magnetic field) which can be measured with unitary *signal-to-noise* ratio and acquisition bandwidth, as in Eq. 4.

$$S = \frac{B_{1,\mathrm{RF\ min}}}{\frac{\mathrm{S}}{\mathrm{N}}\sqrt{\mathrm{BW}}} \tag{4}$$

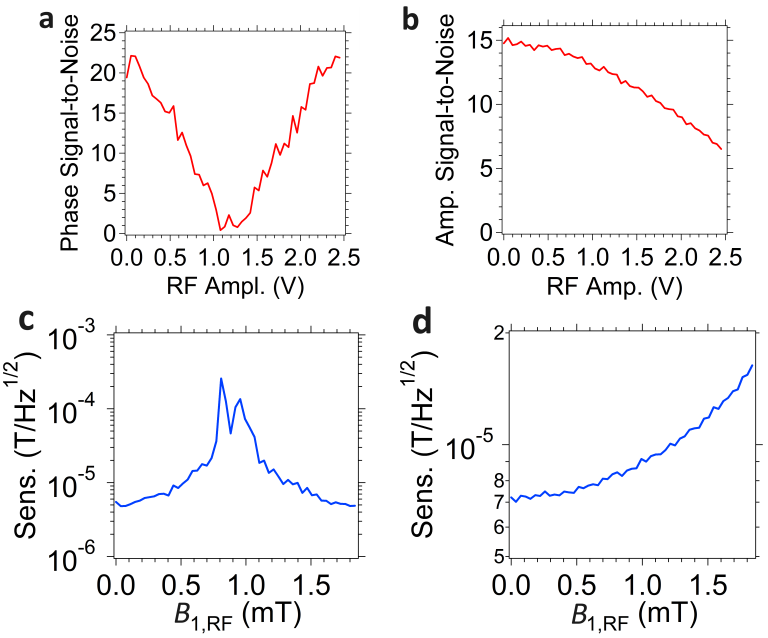

Supplementary Figure 12: Estimation of the *signal-to-noise* ratio (a,c) and of the sensitivity (b,d) for the phase and the amplitude of VO(TPP) (Fig. 2 of main text).

We estimate the minimum RF field according to the discussion reported in the main text, which gives $B_{1,\mathrm{RF\ min}} = 9.8 \cdot 10^{-6}\,\mathrm{T}$ (see main text). The acquisition bandwidth is given by the inverse of the repetition time of the sequence, which is $\mathrm{BW} = 1/(0.02\,s) = 50\,\mathrm{Hz}$. The evaluation of the *signal-to-noise* ratio can be done starting from Fig. 2.c of main text. The noise on the phase signal is estimated by calculating the square root of the average quadratic deviation of the phase from the fit (first and last point are excluded from calculation). The absolute value of the signal (to avoid negative numbers) is then divided by this quantity to get the *signal-to-noise*. This finally allow us to calculate the sensitivity values shown in Supplementary Fig. 12. An estimation of the sensitivity performed using the amplitude of the echo signal of Supplementary Fig. 8 is shown for comparison and lead to similar upper limit for sensitivity. The average sensitivity per unit of volume is then calculated as $S_{\mathrm{V}} = S/\sqrt{\rho}$, with ρ the spin density of the sample [11, 8].

Dynamical Decoupling Sensing Protocol Eq. 4 can be used to estimate the sensitivity also for the Dynamical decoupling sequences. The minimum magnetic field is evaluated as described in the main text, using the derivative of the echo phase a function of the RF magnetic field together with the coil calibration data. Due to the differences in the data, for each curve we take the maximum of the absolute value of each derivative. This gives the optimal point of sensitivity for each tested sequence in the investigated range of applied $B_{1,\mathrm{RF}}$. The concentration sensitivity is again calculated as $S_{\mathrm{conc}} = S/\sqrt{\rho}$. Our estimations and values used are summarized in Table 2 (we have $\mathrm{BW} = 1/t_{\mathrm{rel}} = 1/0.025\,s = 40\,\mathrm{Hz}$ for all measures).

Sequence	τ (μs)	$B_{\min}$ (T)	S/N	S (T Hz$^{-1/2}$)	S_{conc} (T Hz$^{-1/2}\mu$m$^{3/2}$)
CP2	1	$3.7 \cdot 10^{-6}$	88	$6.6 \cdot 10^{-9}$	$2.1 \cdot 10^{-10}$
	1.3	$1.7 \cdot 10^{-5}$	93	$2.8 \cdot 10^{-8}$	$8.9 \cdot 10^{-10}$
	1.7	$1.5 \cdot 10^{-5}$	69	$3.4 \cdot 10^{-8}$	$1.1 \cdot 10^{-9}$
CP3	1	$4.0 \cdot 10^{-6}$	65	$9.8 \cdot 10^{-9}$	$3.1 \cdot 10^{-10}$
	1.3	$6 \cdot 10^{-6}$	47	$2.0 \cdot 10^{-8}$	$6.4 \cdot 10^{-10}$
	1.7	$3.6 \cdot 10^{-6}$	32	$1.8 \cdot 10^{-8}$	$5.6 \cdot 10^{-10}$
CP4	1	$2.1 \cdot 10^{-7}$	57	$5.9 \cdot 10^{-10}$	$1.9 \cdot 10^{-11}$
	1.3	$2.6 \cdot 10^{-7}$	36	$1.1 \cdot 10^{-9}$	$3.6 \cdot 10^{-11}$
	1.7	$2.6 \cdot 10^{-7}$	17	$2.3 \cdot 10^{-9}$	$7.5 \cdot 10^{-11}$
CP5	1	$2.2 \cdot 10^{-7}$	36	$9.6 \cdot 10^{-10}$	$3.0 \cdot 10^{-11}$
	1.3	$1.4 \cdot 10^{-6}$	67	$3.3 \cdot 10^{-9}$	$1.0 \cdot 10^{-10}$
	1.7	$2.7 \cdot 10^{-7}$	12	$2.6 \cdot 10^{-9}$	$8.3 \cdot 10^{-11}$
Sequence	$\#\pi$	$B_{\min}$ (T)	S/N	S (T Hz$^{-1/2}$)	S_{conc} (T Hz$^{-1/2}\mu$m^{3})
PDD	1	$1.6 \cdot 10^{-5}$	114	$2.3 \cdot 10^{-8}$	$7.4 \cdot 10^{-10}$
	2	$1.4 \cdot 10^{-5}$	113	$1.9 \cdot 10^{-8}$	$6.1 \cdot 10^{-10}$
	3	$7.7 \cdot 10^{-6}$	69	$1.8 \cdot 10^{-8}$	$5.6 \cdot 10^{-10}$
	4	$1.6 \cdot 10^{-6}$	51	$5 \cdot 10^{-9}$	$1.6 \cdot 10^{-10}$

Supplementary Table 2: Summary of the values used for evaluating the spin sensitivity for the Carr-Purcell-Meiboom-Gill sequences (CP) and the Period Dynamical Decoupling (PDD) used in this work.

3.3 Estimation of Allan Variance for VO(TPP)

Allan variance is a parameter typically infer the noise and the stability of a sensor [12, 13]. This method relies on the calculation of the two-sample variance of a set of N identical and repeated measures of the same physical quantity, each one with a total measurement time t_{single}. Briefly, the set of N values is divided in K subgroups without overlap, each one containing $m = N/K$ elements. The average value of the physical quantity is evaluated for each K^{th} subgroup. Allan variance is then calculated for the whole dataset as the average quadratic deviation of the average values of each consecutive $K^{th}, (K+1)^{th}$ subgroups. This procedure is repeated for different sizes for the subgroups to build a log-log plot of the Allan deviation as a function of the average time, which depends by the number of Clusters according to $t_{\text{avr}} = m * t_{\text{single}} = N/K * t_{\text{single}} \propto m$ [12, 13]. It's worth mentioning that this method is based on the acquisition of N identical repeated measure of the same quantity (a fixed value of the amplitude or of the phase of the RF magnetic field, in our experiments) and, in order to have a statistical meaning, should be done over a large collection of N samples. An empirical criterion further suggests that each subgroup should have at least 9 data points to have adequate statistical meaning [12, 13]. Under our experimental conditions, each measure results from the average of 2000 individual acquisition, each one essentially taking an acquisition time equal to $t_{\text{relax}} = 15\,\text{ms}$ (total time for each point of $t_{\text{tot}} = 15\,\text{ms} * 2000 = 30\,\text{s}$). The average is done directly by the oscilloscope before the resulting traces are exported and, then, analyzed. Fig. 1.c of the main text suggests us a first way to estimate Allan deviation starting from the linear dependence of the echo phase from the RF field amplitude. We first subtract the linear fit of the phase a function of the magnetic field amplitude (dashed line) from the data points, in order to obtain only the fluctuation of the echo phase with respect to the value expected from the fit. This removes the bias given by the fact that the echo amplitude is linearly changed step-by-step, and allows us to inspect the stability of the measured echo phase. The first and the last point, where the jump between $-90°$ and $+90°$

occurs, are excluded. Allan deviation is then evaluated on this new data set (so, phase values) and, then, converted back to its equivalent field value according to the conversion factor given by the slope of the linear fit. The results are plotted in Supplementary Fig. 13 as a function of the number of points of each cluster (which is proportional to the average time). Error bars are obtained using the relative error discussed in [12].

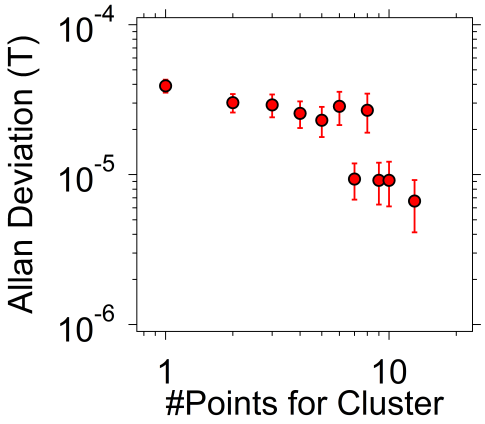

Supplementary Figure 13: Allan deviation as a function of the number of points of each cluster evaluated from the data of Fig. 1.c of the main paper according to the discussion of Sec. 3.3.

The estimated Allan variance values are consistent with the minimum detectable field reported in the main text, which has been estimated independently. The values only slightly changes as a function of the number of points of each cluster corroborating the stability of the sensor at least over a time up to $11 * 30\,\mathrm{s} = 330\,s$, which is much longer than the memory time and the spin-lattice relaxation time. However, as mentioned above, the low number of points of the dataset makes hard to understand the correct statistical significance of these values. It is worth mentioning also that, due to the step-by-step scan of RF field, it is hard to relate this value to the fluctuation of the sensor or of the quantity to be measured.

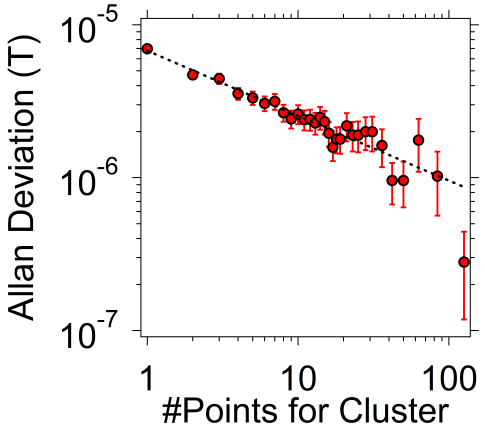

Supplementary Figure 14: Allan deviation as a function of the number of point of each cluster evaluated from the echo phase of a new dataset obtained by repeating the Hahn echo sensing protocol 250 times at fixed $B_{1,\mathrm{RF}} = 1.2 \cdot 10^{-4}\,\mathrm{T}$ and $\phi_{\mathrm{RF}} = 0°$, according to the discussion of Sec. 3.3. Dashed line is a fit based on a power law.

For the reasons above, we better assess our Allan variance by fixing the amplitude of the

RF magnetic field to $B_{1,\mathrm{RF}} = 1.2 \cdot 10^{-4}\,\mathrm{T}$ and $\phi_{\mathrm{RF}} = 0°$, and by taking 250 consecutive acquisitions of the echo signal resulting from the same Hahn echo sensing protocol performed on a VO(TPP) sample with concentration identical to the one used in this work. Here we use a similar superconducting YBCO coplanar resonator, similar RF coil and similar experimental conditions. Allan deviation is evaluated according to the method described in [12, 13] starting from the phase of the measured set of echo signals, and the results is reported in Supplementary Figure 14. The values are consistent (or even slightly better) with the ones reported in Fig. 13 and with the estimation of the minimum detectable field reported in the main text. A fit based on a power law (dashed line) gives an exponent of 0.4 ± 0.1, which suggest that the dominant type of noise under our experimental conditions and investigated range is the white (i.e. thermal) one [13].

3.4 Theoretical Estimation of Sensitivity

Case of Hahn Echo sequence for VO(TPP) We compare our estimation of sensitivity with the theoretical value expected from the model described in [5]. In particular, we base on Eq. (41) of the mentioned reference, which we report in Eq. 5 (for $q = 1$) for better clarity. This is the sensitivity as the minimum detectable signal, S_{min}, that yields unit *Signal-to-Noise* ratio for an integration of time of 1 s.

$$S_{\mathrm{min}} = \frac{e^{\chi(t)}\sqrt{t + t_{\mathrm{opr}}}}{2C(t_{\mathrm{opr}})|\partial p(t)|} \tag{5}$$

We specialize 5 to our experimental case and conditions. In particular the sensing time is chosen as $t = 2\tau$, while the operation time for initializing, manipulating and reading out spins is $t_{\mathrm{opr}} = t_{\pi/2} + t_{\pi} + t_{\mathrm{relax}} \approx t_{\mathrm{relax}} = 15\,\mathrm{ms}$. We choose $\chi(t) = (t/T_{\mathrm{m}})^x = (2\tau/T_{\mathrm{m}})^x$, where $T_{\mathrm{m}} = 1.1\,\mu\mathrm{s}$ and $x = 1.1$ are the memory time and the stretching exponent obtained from the measure of Hahn's echo memory time. We take the conversion efficiency $C(t_{\mathrm{opr}}) = 1$ noticing that this phenomenological parameter had been originally introduced to take into account the collection efficiency of the fluorescence signal in ODMR experiments [8]. The quantity $p(t)$ describes the phase introduced by the AC modulation, which is defined through $p(t) = \phi(t) = \omega t = g\mu_{\mathrm{B}}/\hbar B_{1,\mathrm{RF}}(t)t = g\mu_{\mathrm{B}}/\hbar B_{1,\mathrm{RF}}(t)2\tau$, while its derivative has to be evaluated for the RF magnetic field $B_{\mathrm{RF}}(t)$. This leads to $\partial p(t) = g\mu_{\mathrm{B}}/\hbar 2\tau$. The resulting sensitivity is $S_{\mathrm{min}} \approx 1.5 \cdot 10^{-6}\mathrm{T\,Hz}^{-1/2}$, which correspond to an average concentration per unit volume of $S_{\mathrm{min,vol}} \approx 3.1 \cdot 10^{-10}\mathrm{T\,Hz}^{-1/2}\,\mu m^{3/2}$. These values are consistent with the estimations reported in the main text for VO(TPP).

Case of Dynamical Decoupling for BDPA The models developed in [5] allows us to extend our estimation for the theoretical sensitivity to the case of CP protocol. Following the discussion in [5], we use Eq. 6.

$$S_{\mathrm{min}} = \left(\frac{e^{\chi(t)}\sqrt{t + t_{\mathrm{opr}}}}{2C(t_{\mathrm{opr}})|\partial p(t)|}\right)^{1/2} \tag{6}$$

The terms $\chi(t), t, t_{\mathrm{opr}}$ have the same meaning of Eq. 5, but now the memory time used in $\chi(t)$ is the one obtained for the number of π pulses used (Supplementary Fig. 6) and t is the new total duration of the free precesssion time, $t = 2\tau \cdot \#\pi$. The conversion efficiency $C(t_{\mathrm{opr}})$ is, again, a phenomenological coefficient between 0 and 1, and we assume it to be $C(t_{\mathrm{opr}}) = 1$. We assume a quadratic dependence for the phase variation as a function of $B_{1,\mathrm{RF}}$[5], which gives $p(t) = (g\mu_{\mathrm{B}}t/\hbar B_{1,\mathrm{RF}}(t))^2$ and, then, $\partial p(t) = 2B_{1,\mathrm{RF}}(t)(g\mu_{\mathrm{B}}/\hbar)^2\partial B_{1,\mathrm{RF}}(t) = 2B_{1,\mathrm{RF}}(t)t^2(g\mu_{\mathrm{B}}/\hbar)^3$. The

sensitivity now depends by the working point chosen. We further assume that $B_{1,\mathrm{RF}}(t) = B_{1,\mathrm{RF}} sin(2\pi\nu t) \approx B_{1,\mathrm{RF}} 2\pi\nu t$. We report in Supplementary Fig. 15 the estimations obtained at the magnetic field value at which the maximum phase derivative is found.

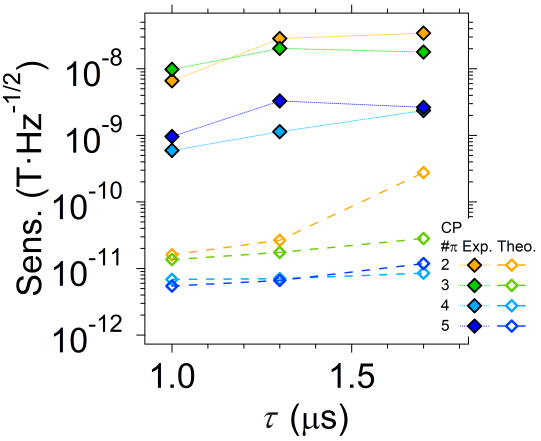

Supplementary Figure 15: Estimation of the theoretical Sensitivity for the CP protocol obtained through Eq.6. Values in Tab. 2 are added for comparison.

The theoretical sensitivity results to be much larger than the one estimated from experimental data. This difference can be attributed to several reasons. Firstly, Eq. 6 is not taking into account the inhomogeneity of the microwave magnetic field generated by the resonator when the pulses are used to drive the spins. This is also affecting the efficiency of the microwave manipulation. Another possible origin of such difference might be the different contest for which the original model was proposed (Optically Detected Magnetic Resonance), with the results that additional corrections might be needed. For instance, the physical meaning and the value of the conversion efficiency in our experimental conditions, which could be $0 < C(t_{\mathrm{opr}}) \leq 1$ and not necessary unitary, might need to be further assessed. Finally, according to the results of Supplementary Fig. 8, we notice that the model described in [5] holds for the cases in which the dependence on the RF magnetic field is a power law with exponents being exactly $p = 1$ or $p = 2$, which differs from our experimental observations.

Supplementary References

[1] Claudio Bonizzoni, Mirco Tincani, Fabio Santanni, and Marco Affronte. Machine-learning-assisted manipulation and readout of molecular spin qubits. *Phys. Rev. Appl.*, 18, 064074 (2022).

[2] Claudio Bonizzoni, et al. Storage and retrieval of microwave pulses with molecular spin ensembles. *npj Quantum Inf.*, 6, 68 (2020).

[3] Claudio Bonizzoni, et al. Coupling sub-nanoliter bdpa organic radical spin ensembles with ybco inverse anapole resonators. *Appl. Magn. Reson.*, 54, 143–164 (2023).

[4] C. Bonizzoni, A. Ghirri, and M. Affronte. Coherent coupling of molecular spins with microwave photons in planar superconducting resonators. *Adv. Physics: X*, 3, 1435305 (2018).

[5] C. L. Degen, F. Reinhard, and P. Cappellaro. Quantum sensing. *Rev. Mod. Phys.*, 89, 035002 (2017).

[6] Masashi Hirose, Clarice D. Aiello, and Paola Cappellaro. Continuous dynamical decoupling magnetometry. *Phys. Rev. A*, 86, 062320 (2012).

[7] M. Alexandre Souza, Gonzalo A. Álvarez, and Dieter Suter. Robust dynamical decoupling. *Philos. Trans. Royal Soc. A: Math. Phys. Eng. Sci.*, 370, 4748–4769 (2012).

[8] J. M. Taylor, et al. High-sensitivity diamond magnetometer with nanoscale resolution. *Nat. Phys.*, 7, 270 (2011).

[9] L. M. Pham, et al. Enhanced solid-state multispin metrology using dynamical decoupling. *Phys. Rev. B*, 86, 045214 (2012).

[10] Aharon Blank, Ygal Twig, and Yakir Ishay. Recent trends in high spin sensitivity magnetic resonance. *J. Magn. Reson.*, 280, 20–29 (2017).

[11] Priyadharshini Balasubramanian, et al. dc magnetometry with engineered nitrogen-vacancy spin ensembles in diamond. *Nano Lett.*, 19, 6681–6686 (2019).

[12] Katarína Draganová, et al. Noise analysis of magnetic sensors using allan variance. *Acta Phys. Polonica A*, 126, 394–395 (2014).

[13] Marin B. Marinov, Borislav Ganev, Nina Djermanova, and Tasho D. Tashev. Analysis of sensors noise performance using allan deviation. In *2019 IEEE XXVIII International Scientific Conference Electronics (ET)*, 1–4 (2019).